Biomechanics Aware Collaborative Robot System for Delivery of Safe Physical Therapy in Shoulder Rehabilitation

J. Micah Prendergast, Stephan Balvert, Tom Driessen, Ajay Seth, and Luka Peternel, *Member, IEEE*

***Abstract*—In this work, we explore using computational musculoskeletal modeling to equip an industrial collaborative robot with awareness of the internal state of a patient to safely deliver physical therapy. A major concern of robot-mediated physical therapy is that robots may unwittingly injure patients. For patients with shoulder injuries this typically means the risk of tearing a rotator-cuff muscle tendon. Risk of reinjury hampers both human and robot therapists and it is the main reason for conservative physical therapy. Advances in human musculoskeletal modeling, however, can equip robots with additional perception of potential reinjury risks. While the ultimate goal is to improve the safety, range-of-motion and activity that patients receive through robot-mediated therapy, the aim of this letter is to develop and test a framework that enables the robot to understand the state of the patient and to execute physical therapy movements that demonstrate low injury risk and achieve a large range-of-motion in human subjects. We build on prior work in human-robot interaction via impedance control, but take robot awareness of the human to the next level by including and manipulating a musculoskeletal model in parallel to the patient. Taking the most common shoulder impairments (i.e., rotator-cuff tears) as an example, we demonstrate planned, model-based trajectories that minimize strain in these muscles and corresponding robot-mediated movements on healthy subjects. Our experiments suggest that musculoskeletal awareness is a promising approach to plan and deliver therapeutic movements that are safe and effective via an industrial robot.**

***Index Terms*—Human-robot interaction, model-based awareness, physical therapy robot, musculoskeletal modeling, OpenSim.**

I. Introduction

To exploit the benefits of human-robot interaction particularly in patient-directed therapy, robots must perceive the state of the patient and his/her injury risks. In this letter, we focus on physical therapy intensive recovery from rotator-cuff injuries of the shoulder as a clinically motivated driving problem. Shoulder rotator-cuff tears alone have an estimated rate of 22.1% in the general population and over 50% for those older than 60 [1].

Manuscript received February 24, 2021; accepted June 24, 2021. Date of publication July 16, 2021; date of current version July 28, 2021. The work of J. Micah Prendergast was supported by the 3mE Cohesion Grant from Delft University of Technology. *(Corresponding author: J. Micah Prendergast.)*

The authors are with the Biomechanical Engineering and Cognitive Robotics Departments, Delft University of Technology, 2628, CD Delft, Netherlands (e-mail: j.m.prendergast@tudelft.nl; s.balvert@student.tudelft.nl; t.driessen-1@student.tudelft.nl; a.seth@tudelft.nl; l.peternel@tudelft.nl).

Digital Object Identifier 10.1109/LRA.2021.3097375

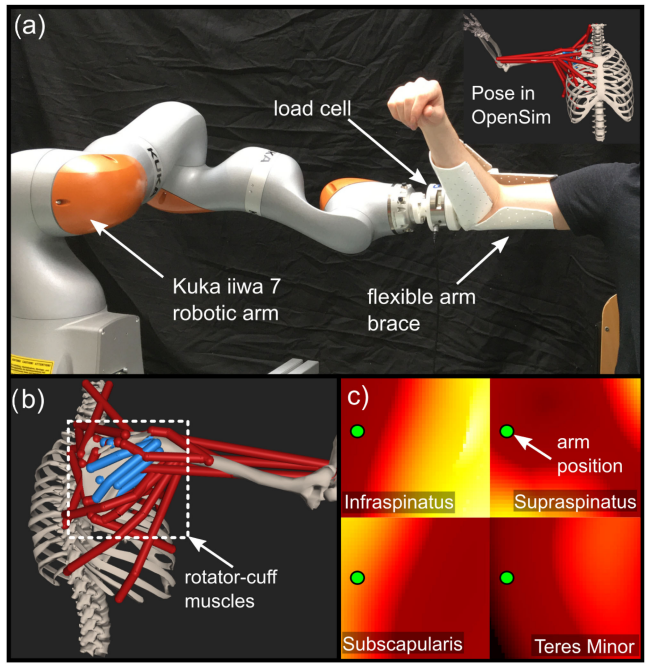

Fig. 1. Physical system and biomechanical simulation setup. (a) A Kuka LBR iiwa robotic manipulator delivers motion to the shoulder of a test subject through an elbow brace and load cell attachment. (b) An OpenSim biomechanical model of the shoulder matches the movement of the subject and strains in the rotator-cuff muscles (highlighted) are estimated. (c) The estimated strains of the individual rotator-cuff muscles presented as 2D heatmaps over the shoulder range of motion (axes).

Either following injury or after surgical repair, a lengthy period of physical therapy is necessary to restore shoulder mobility.

Due to the complexity of the shoulder and risks of re-injury physical therapy of the shoulder remains conservative and performed by human physiotherapists [2]. The conservative nature of physiotherapist means that the amount of therapy delivered is limited and there are many more patients than available physiotherapists at any given time. Furthermore, the work can be quite laborious for the physiotherapists. A promising alternative to classic physiotherapist-based rehabilitation is robotic rehabilitation [3], [4].

Several upper-extremity rehabilitation devices have been developed [3], [4], but they are highly specialized and bulky mechanical systems that are expensive and hard to move between patients, which severely limits clinical access to therapy. In

addition, to the best of our knowledge, these existing devices do not target the physical therapy requirements of a recovering rotator-cuff tear. On the other hand, mass-produced industrial collaborative robots are already certified to safely interact with humans, are less expensive, and more generally applicable compared to highly specialized rehabilitation devices. Therefore our system aims to retool an off-the-shelf collaborative robotic arm to safely and effectively deliver physical therapy to the human shoulder in the case of the most common rotator-cuff injuries.

When applying physical human-robot interaction (pHRI) for human movement rehabilitation, impedance control offers significant benefits, enabling the modulation of interaction dynamics in real-time through a spring-mass-damper model [5]. Through this impedance control approach the stiffness of the robotic device can be decreased or increased based on the desired rehabilitation strategy or training intensity [6]–[8]. This method also enables the robot to be soft in certain directions, while being stiff in the other directions, allowing the robot to act as a guide for the human. Additionally, the formulation enables easy incorporation of gravity compensation terms for the human arm. Nevertheless, impedance control on its own, usually cannot guarantee the safety of the human with which the robot is interacting.

Past research on safety in pHRI has primarily focused on external safety, i.e., collision detection and avoidance [10], [11], awareness of potential injury due to external collisions [12], [13], and conservative force/velocity limits [14]. In [13], the authors proposed a safety map, which relates biomechanics injury data to the instantaneous collision dynamics and parameters of the robot and the subject in task-dependent workspace sets. In contrast to industrial applications, in rehabilitation-related pHRI the critical safety concern is not external collisions but internal properties related to the functioning of the body (e.g., range of motion of joints, joint torques, tendon strains, muscle forces, etc.).

To effectively deliver physical therapy to human patients, robots have to maximize therapy time and range of motion [15] but at the same time have to make sure they stay within the human safety margins (muscle strains, etc.) with respect to the current state of rehabilitation. To do this, they have to be more perceptive of the patient and his/her injury risks. While it is certainly necessary to imbue the robot with sensors to carefully observe the patient, it is not enough. Injury risks in physical therapy involve loads and strains of internal structures and tissues (i.e, muscles, tendons and ligaments, etc.), which cannot be directly observed by external measurements.

Recently, pHRI research started to focus on internal safety, where the robot control system includes human biomechanical and musculoskeletal models. These models can account for patient-specific parameters and give an accurate estimate of the internal properties of the human body. Some of the properties that have been considered are (static) joint loading [16], muscle fatigue [17], muscle comfort [18], and muscle manipulability [19]. However, these methods were mostly designed for non-rehabilitation related applications, such as human-robot collaboration in industrial tasks [16]–[18] and use of exoskeleton for power-assist [19].

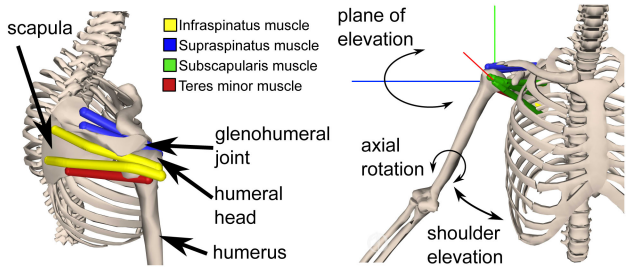

Fig. 2. Biomechanical model of the shoulder [9] with only the rotator-cuff muscles visible for clarity (left). Shoulder joint coordinate system (at glenohumeral joint center) and the degrees-of-freedom: plane of elevation, shoulder elevation and axial rotation of the humerus are shown (right).

A few recent studies focused on using off-the-shelf collaborative robotic arms for shoulder rehabilitation. The method in [20] used collaborative robotic arm for upper arm rehabilitation and proposed to gather physical (force, position, etc.) and psychophysiological (EMG, EEG, etc.) measurement data from various sensory systems. The method in [21] similarly used a collaborative robotic arm to perform shoulder rehabilitation, where the control was based on the measurement of arm pose and muscle activity through electromyography. However, these methods did not incorporate biomechanical models of the human arm and therefore had limited knowledge of the internal musculoskeletal system of the human arm. Without accurate perception of these complex internal dynamics, injury risks during robotic physical therapy can not be properly mitigated. In addition, these methods also did not target rotator cuff injuries and physiotherapy.

To address this issue, we propose a new physiotherapy system for rotator cuff injuries, based on a collaborative robot that incorporates a patient-specific biomechanical model to inform robotic trajectory planning, patient state estimation and impedance control. This integration of musculoskeletal modeling within the system allows it to plan therapy trajectories to reduce the strain of targeted muscles and tendons, while enabling increased mobility of the human arm in terms of range of motion.

A critical component of this system is the *strain map* (Fig. 1 c), which we have developed to provide the muscle strains of each of the rotator-cuff muscles at any pose of the subject's arm. These strain maps allow us to integrate muscle strain estimates from the biomechanical model (see Fig. 2) into the robotic path planning and control system and enable quantitative feedback to the system about safety/injury in any patient pose. If strains in the muscles are exceeded, a healing muscle/tendon might be re-injured. While a human physiotherapist has only qualitative sensing and no direct access to the muscle strains, they are limited to more conservative movements to avoid re-injuring the healing muscles. By using these strain maps, the proposed robotic system gains quantitative insight into a subject's muscles strains, allowing it to safely maneuver a subject through less conservative, larger range of motion exercises.

In addition, the biomechanical model is complemented by external measurements to augment the estimates of the model. This allows for real-time model updates, and more accurate perception and control of the complete robotic system, for safe delivery of robotic physiotherapy. In this work, we present the

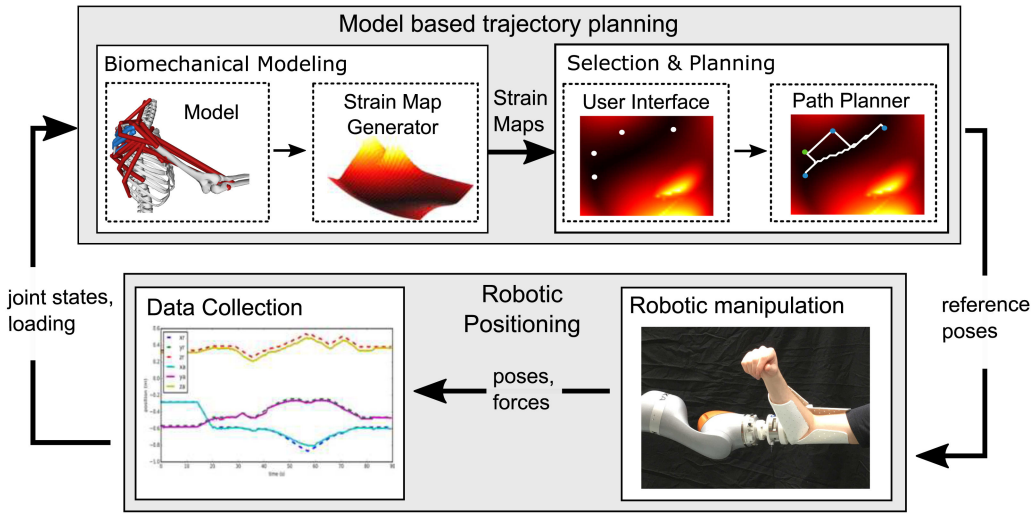

Fig. 3. Workflow of the biomechanics aware robotic system for delivering physical therapy. The biomechanical model is used to generate maps of muscle strains. A simple point selection and planning interface enables the user to select start, end and waypoints in joint space. A low strain path is computed over the strain map and transformed into an endpoint reference frame that the robotic manipulator can follow at a user-selected speed. Robot position and force measures are fed back to the biomechanical model to update its current state. Data is collected from the robot for further evaluation.

development of these shoulder muscle strain maps according to which the optimization algorithm plans the trajectories. The system is demonstrated and evaluated with proof of concept experiments on a Kuka LBR iiwa collaborative robot.

II. Methodology

The methodology is divided into three subsections (see Fig. 3 for an overview). A) Presents the use of the biomechanics modeling tools in the development of the shoulder strain maps. B) Establishes the safe path planning technique implemented by the proposed system for navigating these strain maps. C) Explains the transition of these strain map paths to the physical space of the robotic system and highlights the impedance control law used for safely tracking these target trajectories.

A. Strain Map Computation

To accurately model the internal strains of a subject's shoulder, the open-source computational musculoskeletal modeling tool OpenSim is used. This software allows for biometrically scaled subject models to be created and analyzed at a high degree of fidelity and under all manner of physical input dynamics (both internal from the muscle activations themselves and external). For the purposes of this work, the primary goal is to inform the robot of the tendon strain on each of the four rotator-cuff muscle tendons (strain map) throughout the range of motion of the subject (see Fig. 4). This strain space is obtained using OpenSim [22] and the Thoracoscapular Shoulder Model [9]. To generate muscle strain map, the proposed approach requires position and velocity of the shoulder model (joints) and the applied loads and their location.

As the rotator-cuff muscles span the glenohumeral joint we consider only the three degrees of freedom that comprise the motion of the humerus (upper arm) relative to the scapula (shoulder blade). These include: shoulder elevation, with a range of motion from −44 to 144 degrees; the plane in which the arm is moved (referred to as plane of elevation throughout), also known as horizontal abduction, with a range from −85 to 180 degrees;

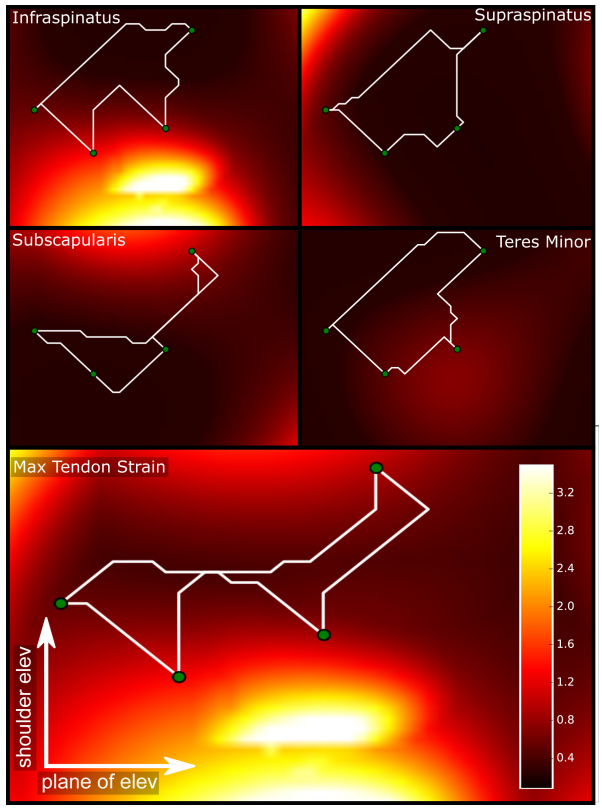

Fig. 4. Tendon strain maps represented by a heat spectrum. Four individual rotator-cuff muscle tendon strains (upper graphs) and total combined (lower graph) were used to plan motions that reduce the potential strain on one or multiple tendons. Path indicates different motion paths for identical starting pose and intermediate points, when different muscle tendons are prioritized.

internal and external (axial) rotation, with a range from -90 to 90 degrees (see Fig. 2).

To reduce computational costs during real-time operation, complete strain maps are computed throughout the entire range of motion for each muscle and at varying speeds and muscle activation off-line. For this computation, the humerus was posed in every possible combination of the selected three degrees of freedom of the glenohumeral joint, using 4° increments. The speed of the arm and the level of activation of all four of the rotator-cuff muscles were set. The muscle and tendon are allowed to reach equilibrium according to

$$f_o^M(a\mathbf{f^L}(l^M)\mathbf{f^V}(v^M) + \mathbf{f^{PE}}(l^M))cos\alpha - f_o^M\mathbf{f^T}(l^T) = 0, \tag{1}$$

where $\mathbf{f^L}$, $\mathbf{f^{PE}}$, $\mathbf{f^T}$ are the active force-length curve, passive force-length curve and tendon force-length curve respectively, $\mathbf{f^V}$ is the force-velocity curve, a is the muscle activation, α is the pennation angle, l^M is the muscle fiber length, v^M is the muscle velocity, and l^T is the tendon length and f_o^M is the max isometric force. The muscle fiber length at equilibrium is then used to determine the normalized muscle fiber force which is then used to obtain the tendon length from the normalized tendon force-length curve as detailed in [23]. The tendon length and tendon slack length l^o are then used to compute percent tendon strain ε as

$$\varepsilon = \frac{l^T - l^o}{l^o} \cdot 100\% \tag{2}$$

Note that for the purpose of physical therapy after a rotator-cuff tear, in this study we assume low muscle activation as the subject is expected to be fully relaxed throughout the motion. We precompute activated strain maps in anticipation of the next phase of therapy involving low levels of activity such that the measured input forces between the subject and the robot end-effector can be used as feedback and for map/trajectory updates.

Within the biomechanical shoulder model, the infraspinatus muscle is divided into an inferior and a superior part, the supraspinatus muscle into an anterior and a posterior part and the subscapularis muscle into an inferior, medial and superior part, while the teres minor muscle is not divided. In determining the strain of each of the rotator-cuff muscle tendons, the strains of those parts were compared for each muscle at each position and the highest strain value was taken to be representative of the strain of the entire muscle tendon. This way, the strain space includes the highest possible strain the tendon will undergo at any given position.

In addition, we reduce the size of our map to include only feasible poses (-20–160 degrees for plane of elevation and 0-144 degrees for shoulder elevation). Once these maps have been computed for the subject, they are then stored in the system for use by the robot in the planning and control operations during therapy.

B. Safe Path Planning

With strain space maps computed for each of the four rotator-cuff muscles, these maps can be utilized to plan trajectories that avoid large strains in one or more muscle tendons (see Fig. 5).

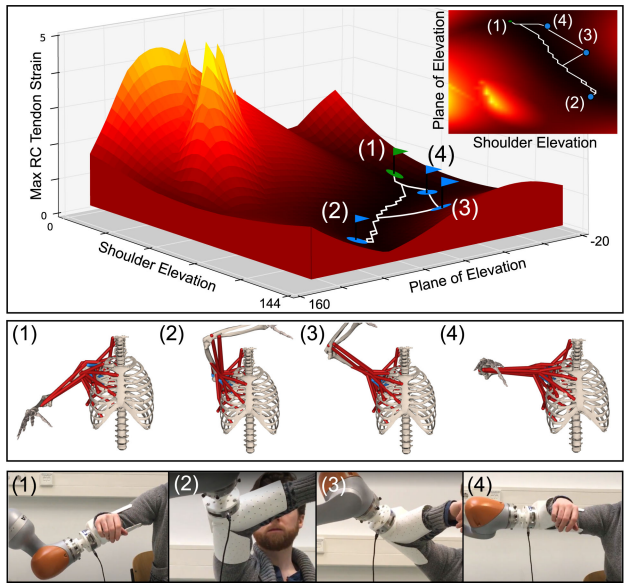

Fig. 5. Example of a low tendon-strain trajectory of the shoulder within the 3D strain map set by a user-specified start point (1) and three waypoints, flags (2), (3), and (4). Inset is a top-down view. Corresponding configurations of the biomechanical model are shown in the middle row and the actual human arm configurations as controlled by the robotic manipulator are captured in the bottom row.

To avoid the task of manually selecting safe paths within these maps, we automate this procedure using a weighted A* approach to path generation [24]. A strain threshold (2 percent strain for the results presented here) is first set, which will denote the barrier within the 3D map. This threshold is easily changed to accommodate more/less restrictive strain limits when that is desired. Regions above this threshold cannot be selected as starting points or waypoints, and the path planner will not cross these barriers.

With the barrier map determined, it is possible to run A* to find the shortest path between any two points within the strain space, however because our goal is to avoid straining the tendons while increasing range of motion, we modify A* to plan trajectories that result in reduced accumulated strain throughout the entire trajectory. This results in generally longer paths with reduced accumulated strain. To accomplish this, we define the distance between each adjacent node within the map by the strain of that node, ε_n. In addition, to allow for A* to continue traversing the strain map towards the end goal, we define a strain distance heuristic. While conventional A* typically uses the Euclidean distance, d_{euclid} as this heuristic, to accommodate our strain weighted method, we multiply by the mean of the strain ε_{mean} within the strain map as a gross estimate of the strain likely to be experienced via a straight-line path to the way-point/goal. The accumulated strain of each node $g(n)$ in the path along with this strain distance estimate from the end goal $h(n))$ allows us to assert a cost $f(n)$ associated with each new node explored in the path.

$$f(n) = g(n) + h(n), \tag{3}$$

$$g(n) = \sum_{i=1}^{n} \varepsilon_i, \tag{4}$$

$$h(n) = \varepsilon_{mean} \cdot d_{euclid}. \tag{5}$$

While this weighted A* approach allows us to automate the path planning procedure, A* will still tend towards relatively short paths between start and goal points. To improve the range of motion while still allowing for low strain paths, the user can select any number of waypoints within the map (see Fig. 5). A* is then run between each point until the path is complete to generate a complete, larger range of motion trajectory.

C. Trajectory Implementation and Control

Once a path has been chosen in the strain map, this path must be transformed to the physical space of the robotic manipulator to allow for implementation of the planned trajectory. To accomplish this, some prior information is necessary about the starting pose of the human relative to the robot base frame, as well as the arm length of the human. Subject specific data (arm length, torso height) is entered along with the starting pose of the human in the robot's X,Y frame and the starting rotation of the human body. For the tests presented here the X,Y position of the subject has been fixed and the rotation of the subject is either facing towards the robot's X axis, or rotated 90 ° and facing in the direction of the robot's Y axis. This allows testing paths that fall within the extreme limits of the subjects planer elevation range of motion.

Once all subject-specific data has been entered and a path has been generated, the path is then transformed into the robot's base frame coordinates. Reference frames are first generated to maneuver the robot's endpoint in a straight line path to the subject's starting position. To simplify this starting procedure, the initial arm pose of the patient is always fixed with the elbow at 90 degrees of shoulder elevation (parallel to the floor) and facing in the direction of the robot's X axis.

Next, the planned path trajectory is generated to maneuver the patient's arm through the prescribed path generated by the weighted A* algorithm. Because the initial path planned is at the resolution of the strain map (4 degrees for the tests presented here), linear interpolation is done between each node in the path prior to the path being transformed to the robot's (Cartesian) task space. The robot itself operates with a set update rate of 200 Hz, thus the speed of the path is dependent on the number of reference transforms provided between each node. This speed is set prior to the initial path planning and is fixed at 5 degrees/second for the tests demonstrated here.

The generated trajectory was controlled by a Cartesian impedance controller [5] defined as

$$\boldsymbol{F}_{ext} = \boldsymbol{K}\left(\boldsymbol{x}_d - \boldsymbol{x}_a\right) + \boldsymbol{D}\left(\dot{\boldsymbol{x}}_d - \dot{\boldsymbol{x}}_a\right), \tag{6}$$

where $\boldsymbol{F}_{ext} \in \mathbb{R}^6$ is the interaction force vector acting from the robot on the environment, $\boldsymbol{K} \in \mathbb{R}^{6\times6}$ and $\boldsymbol{D} \in \mathbb{R}^{6\times6}$ are the desired stiffness and damping matrices in Cartesian space, respectively, while $\boldsymbol{x}_a \in \mathbb{R}^6$ and $\boldsymbol{x}_d \in \mathbb{R}^6$ are the actual and the reference pose vectors of the robot endpoint, respectively. We then controlled the desired interaction force in Cartesian space by the joint torques as

$$\boldsymbol{\tau} = \boldsymbol{M}(\boldsymbol{q})\ddot{\boldsymbol{q}} + \boldsymbol{C}(\boldsymbol{q},\dot{\boldsymbol{q}})\dot{\boldsymbol{q}} + \boldsymbol{g}(\boldsymbol{q}) + \boldsymbol{J}(\boldsymbol{q})^T\left(\boldsymbol{F}_{ext} + \boldsymbol{F}_c(\boldsymbol{q}_h)\right), \tag{7}$$

where $\boldsymbol{\tau} \in \mathbb{R}^7$ is a vector of robot joint torques, $\boldsymbol{q} \in \mathbb{R}^7$ is a vector of robot joint angles, $\boldsymbol{g} \in \mathbb{R}^7$ is the gravity vector, and $\boldsymbol{J} \in \mathbb{R}^{6\times7}$, $\boldsymbol{M} \in \mathbb{R}^{7\times7}$ and $\boldsymbol{C} \in \mathbb{R}^{7\times7}$ are the robot Jacobian matrix, mass matrix, and Coriolis and centrifugal matrix, respectively. $\boldsymbol{F}_c \in \mathbb{R}^6$ is a force vector used to compensate the gravity acting on the human arm and is dependent on the current configuration of the human shoulder $\boldsymbol{q}_h$.

The joint torques $\boldsymbol{\tau}_h \in \mathbb{R}^3$ induced into the human shoulder[1] by the robot endpoint force $\boldsymbol{F}_{ext}$ were as

$$\boldsymbol{\tau}_h = \boldsymbol{J}_h(\boldsymbol{q}_h)^T\left(\boldsymbol{F}_{ext} + \boldsymbol{F}_c(\boldsymbol{q}_h)\right), \tag{8}$$

and can be used as an input for the musculoskeletal model. Note that due to the slow velocity of the arm for all applied motions, we make the assumption that this is quasi-static. The human arm Jacobian matrix $\boldsymbol{J}_h \in \mathbb{R}^{6\times3}$ and human arm configuration $\boldsymbol{q}_h \in \mathbb{R}^3$ defined this transformation. In addition, the human shoulder configuration $\boldsymbol{q}_h$ can be calculated through the kinematic model of the shoulder based on the measured robot endpoint pose, which coincides with the human elbow pose.

The stiffness matrix can be non-diagonal and has principal axes rotated with respect to the robot base frame to regulate the stiffness in arbitrary directions. The equally rotated damping matrix was obtained by a *double diagonalisation design* [25] depending on the current stiffness matrix as

$$\boldsymbol{D} = 2\boldsymbol{Q}\boldsymbol{D}_\xi\sqrt{\boldsymbol{K}_0}\boldsymbol{Q}^T, \tag{9}$$

where $\boldsymbol{Q} \in \mathbb{R}^{6\times6}$ and $\boldsymbol{K}_0 \in \mathbb{R}^{6\times6}$ are eigenvectors and eigenvalues obtained by the eigendecomposition of stiffness matrix $\boldsymbol{K} = \boldsymbol{Q}\boldsymbol{K}_0\boldsymbol{Q}^T$. The diagonal matrix $\boldsymbol{D}_\xi \in \mathbb{R}^{6\times6}$ contains damping factors, which were set to 0.7.

III. Experiments

A. Experimental Setup

The presented research was approved by the Human Research Ethics Committee of Delft University of Technology. To evaluate the concept of robotic manipulation of the human arm through the strain space, an arm brace was designed to mount to the robotic manipulator and interface with the human arm. This brace is comprised of a 6-axis load cell (FTS-Delta SI-330-30, Schunk GmbH & Co. KG, Germany), and a soft molded thermoplastic for orthopaedic splinting. In addition, two 3D printed mounts allow for interfacing between the thermoplastic brace and the load cell, and between the load cell and the robotic endpoint. Velcro straps are used to fasten the arm brace to the subjects arm. The entire brace mounts to the endpoint such that the humerus is axially aligned with the endpoint rotation, thus any axial rotation of the shoulder can be directly controlled by the endpoint actuation.

In total, two healthy subjects were tested in these proof-of-concept experiments. Prior to each test, the path planner

[1] Shoulder typically has more degrees of freedom, however, in this study we used the main three involving rotator-cuff muscles.

was adjusted to fit the shoulder height and humerus length of each subject. Strength scaling has little effect because the movement of the subject is expected to be primarily passive. Each test trajectory shown was done with and without a subject to demonstrate the impact of the subject's arm on the ability of the robot to track the reference trajectory. Conducting tests without a subject also allows for confirming that the robot would be capable of completing the reference trajectory. Once this initial run has been conducted, the subject was positioned at the previously set starting pose. The experimenter would then initiate the trajectory via a keyboard interface. Once the robot reaches the initial starting pose for the subject, it maintains this pose until commanded to continue. The subject would then place their arm in the brace and was next instructed to relax their shoulder and to place the full weight of their arm onto the brace, while maintaining an upright position. Once the subject was relaxed and comfortable, the experimenter would initiate the test trajectory. This trajectory could be paused or aborted completely at any time, but this was not necessary for any of the experiments shown.

Once each trajectory was completed, the subject was helped out of the arm brace. Reference pose, actual pose, and force data were saved for post processing and evaluation.

B. Results

Several metrics were used to validate the utility of the proposed physiotherapy system. Positional tracking accuracy, total accumulated path strain, max estimated strain, and reaction forces were all measured and/or calculated to assess the ability of the system to safely plan and execute trajectories utilizing the biomechanics model, strain path planning and impedance control system.

For this evaluation, we highlight four different trajectories, each test with and without a subject present. Trajectory (1) is a point-to-point path over a long range of motion. At the end of this trajectory, the subject intentionally resisted the robotic motion slightly (simulating a non-compliant patient). While this does not result in any unsafe reaction from the system, it does cause the trajectory to deviate from the target path as is expected by the impedance controller.

Trajectories (2) and (3) demonstrate two similar sets of waypoints selected at different axial rotation starting positions (2) at 0 degrees, and (3) at -40 degrees of axial rotation. This can be seen by the different heatmaps in the top right and bottom left images appearing in Fig. 6.

Finally, trajectory (4) demonstrates the tendency of the path planner to move towards the low strain point on the map, retracing along the initial path it finds rather than taking the shortest distance between the top two waypoints.

Max strains expected during these trajectories and the total expected accumulated strain are shown in Table I. These expected strains using the weighted A* approach are compared to trajectories planned by the conventional A* algorithm and generally show lower total path strains throughout. Weighted A* and conventional A* approaches are denoted as W-A* and C-A* respectively in I.

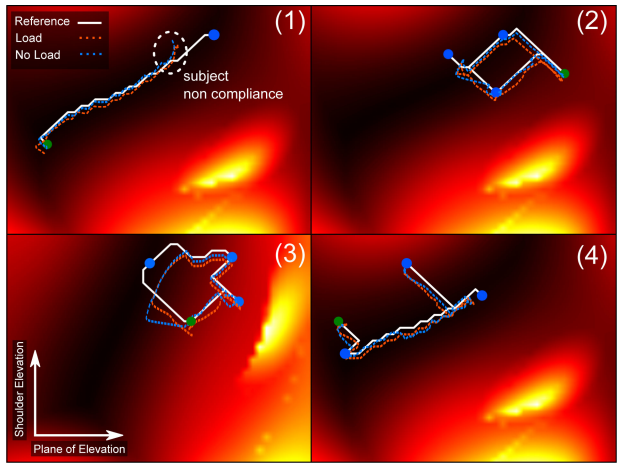

Fig. 6. Varying shoulder trajectories maintaining low-strain for four different conditions: (1) two point trajectory with non-compliance, (2) 0° axial rotation starting pose, (3) $-40°$ axial rotation starting pose and (4) large range of motion are each projected on their respective strain map corresponding to their starting axial-rotation pose. The two paths shown correspond to executed robot trajectories with and without the subject.

TABLE I
WEIGHTED A* VS. CONVENTIONAL A*: MAX AND ACCUMULATED STRAINS

Test	Max C-A*	Max W-A*	Total C-A*	Total W-A*
1	0.64	0.45	11.79	10.47
2	0.93	0.93	23.10	22.29
3	0.82	0.82	24.38	22.66
4	0.98	0.98	22.38	19.38

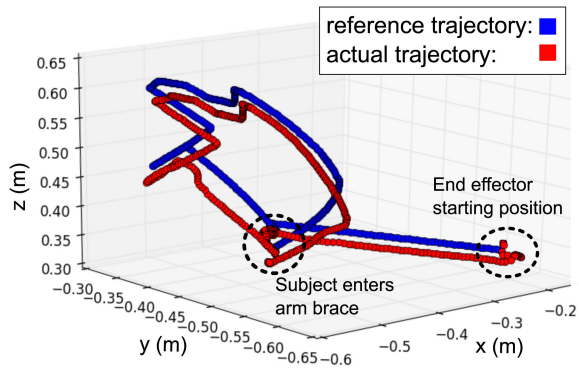

Fig. 7. 3D view of test (3) shown from start to finish. This includes the initial starting pose of the end effect, the mounting of the arm brace on the subject's arm, and the complete trajectory in 3D space.

Fig. 6, shows all four sample trajectories highlighted within their respective strain maps at a fixed axial rotation (for ease of visualization), along with the actual trajectories measured by the robotic arm with and without the applied load of the subject's arm. Fig. 7 shows endpoint trajectory (3) in 3D space and Fig. 8 shows all four trajectories in x,y,z components. As shown, the tracking errors were generally very low for the unloaded case and increased slightly (typically less than 3 cm) for the loaded case. Note the initial motion of the endpoint as the subject enters the arm cuff.

As shown in Table II These errors were not significant enough to substantially increase the strain experienced by the subject

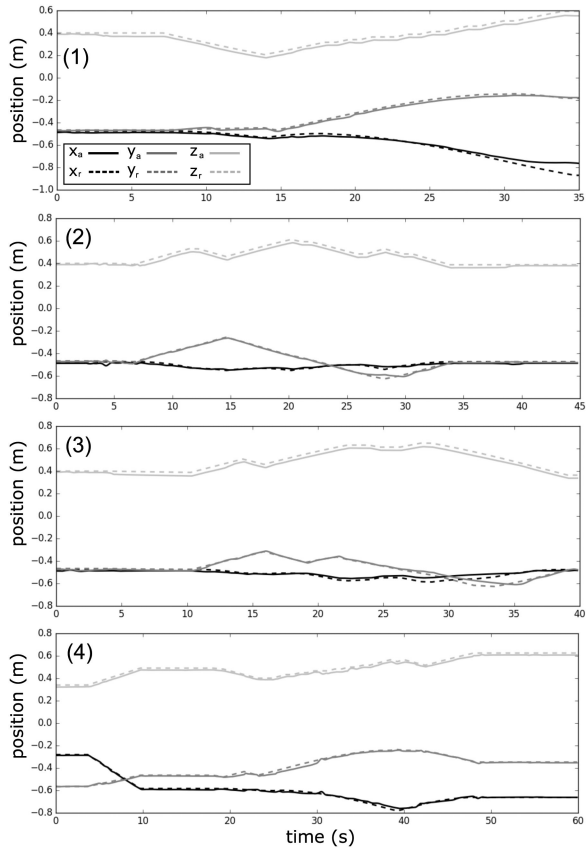

Fig. 8. Four different trajectories from tests (1), (2), (3), and (4). The two resulting paths in x, y and z axes correspond to the reference trajectory given and the actual trajectory followed by the endpoint.

TABLE II
ACTUAL MAX AND ACCUMULATED STRAINS

Test	Max Weighted Actual	Total Weighted Actual
1	0.42	9.00
2	0.92	18.73
3	0.85	21.94
4	0.74	13.28

during the trajectory and did not result in the subject undergoing any large peak strains at any point during the exercise. Finally, the force data is shown for two of these example trajectories in Fig. 9. All force data is transformed into the starting axial rotation pose of the trajectory such that forces acting in the downward direction will be fully resolved into the z direction of the endpoint, once the trajectory begins. No large reaction forces were measured during any tests. In general these forces stayed at or below the 40 N force expected from the relaxed weight (approximately 4 kg) of the subject's arm.

IV. DISCUSSION

There are several key benefits to our proposed approach. The model and corresponding strain maps provide novel information about how to tune end-point stiffness when interacting with patients. Impedance and task-space control formulations enable us to manipulate the endpoint stiffness in varying directions, but

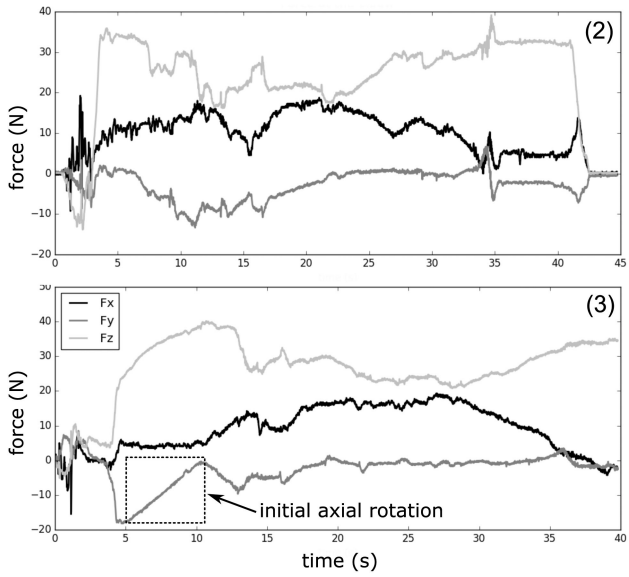

Fig. 9. Measured forces for tests (2) and (3). Note that test (3) involves an initial axial rotation about the endpoint/humerus of −40 degrees. All forces are displayed in the starting frame of the endpoint (after it has reached the starting pose) such that downward forces on the arm brace are in the z-axis of the endpoint coordinates.

the strain map gradients provide the directions needed to orient the endpoint stiffness such that the robot resists movement along lines of increasing strain and is compliant in the direction of decreasing strain.

The use of an industrial collaborative robot for delivery of physiotherapy also has significant benefits. While a custom-built exoskeleton/robot might have several advantages (larger RoM, higher payload, more DoF) [26], [27] and the option to optimise the mechanical design for a specific task and kinematic constraints [28], mass-produced industrial collaborative robots are typically less costly and more readily available compared to custom-built exoskeletons. Furthermore, such robots require little additional training and include rigorous safety features for human-robot interaction.

While we have successfully demonstrated how a collaborative robot can be imbued with biomechanical awareness to guide physical therapy movements in healthy subjects, there are some limitations that must be addressed before attempting to transfer this technology to patients.

One limitation is the unknown accuracy of model estimated rotator-cuff strains. While the model was compared to motion and muscle activity in healthy individuals, it has not been applied, yet, to the specific problem of estimating the strains of the rotator-cuff muscles. Validation of this model from multi-subject experiments is one of the most important steps we will undertake to further the goals of this system.

For this initial study we have limited induced therapy to passive movements where the subject allows the robot to maneuver their arm without actively resisting. While this represents the earliest stages of therapy, later in recovery, patients must begin to increase the activation of their muscles. With this in mind, future work will focus on planning rehabilitation exercises that safely allow for greater muscle activity and forces.

While our model is capable of capturing the kinematics of the scapula given sufficient measurements, the scapula degrees of freedom were not tracked in this initial study. Our focus was on the glenohumeral joint since its degrees of freedom directly affect rotator-cuff muscle strains. Future work focused on larger range of motion activities will need to better account for the scapula pose. We are currently exploring methods using inertial measurement units (on the acromion and sternum) and machine vision to track scapula movement during physical therapy.

In the interest of patient engagement and safety, we continue to explore interfaces such as grips and joysticks to easily engage or disengage the system, or a manual override by releasing their grasp. In this case, the robot returns the patient to a neutral pose. The same action would be executed if muscle strain and/or robot endpoint forces are above specified thresholds.

We have presented a novel approach to biomechanically aware robotics that puts safety and injury to a patient's internal structures at the forefront of robot control. It is a critical first step to exploit industrial robots for the safe delivery of physical therapy to patients. The next steps are clinical studies to verify and enhance patient safety, but more importantly for patients, to evaluate and improve the efficacy of robot-mediated physical therapy. Further future work can focus on extending the approach to other joints.

REFERENCES

[1] H. Minagawa *et al.*, "Prevalence of symptomatic and asymptomatic rotator cuff tears in the general population: From mass-screening in one village," *J. Orthopaedics*, vol. 10, no. 1, pp. 8–12, 2013.

[2] T. Proietti, V. Crocher, A. Roby-Brami, and N. Jarrasse, "Upper-limb robotic exoskeletons for neurorehabilitation: A review on control strategies," *IEEE Rev. Biomed. Eng.*, vol. 9, pp. 4–14, Apr. 2016.

[3] L. Marchal-Crespo and D. J. Reinkensmeyer, "Review of control strategies for robotic movement training after neurologic injury," *J. Neuroeng. Rehabil.*, vol. 6, no. 20, pp. 1–15, 2009.

[4] A. S. Niyetkaliyev, S. Hussain, M. H. Ghayesh, and G. Alici, "Review on design and control aspects of robotic shoulder rehabilitation orthoses," *IEEE Trans. Hum.-Mach. Syst.*, vol. 47, no. 6, pp. 1134–1145, Dec. 2017.

[5] N. Hogan, "Impedance control - An approach to manipulation. I. - Theory. II - Implementation. III - Applications," *ASME Trans. J. Dyn. Syst. Meas. Control B*, vol. 107, pp. 1–24, Mar. 1985.

[6] S. Hussain, P. K. Jamwal, M. H. Ghayesh, and S. Q. Xie, "Assist-as-needed control of an intrinsically compliant robotic gait training orthosis," *IEEE Trans. Ind. Electron.*, vol. 64, no. 2, pp. 1675–1685, Feb. 2016.

[7] A. U. Pehlivan, D. P. Losey, and M. K. O'Malley, "Minimal assist-as-needed controller for upper limb robotic rehabilitation," *IEEE Trans. Robot.*, vol. 32, no. 1, pp. 113–124, Feb. 2016.

[8] C. Wang, L. Peng, Z. G. Hou, W. Wang, and T. Su, "A novel assist-as-needed controller based on fuzzy-logic inference and human impedance identification for upper-limb rehabilitation," in *Proc. IEEE Symp. Ser. Comput. Intell.*, 2019, pp. 1133–1139.

[9] A. Seth, M. Dong, R. Matias, and S. Delp, "Muscle contributions to upper-extremity movement and work from a musculoskeletal model of the human shoulder," *Front. Neurorobot.*, vol. 13, no. 9, pp. 1–9, Nov. 2019.

[10] S. Haddadin, A. De Luca, and A. Albu-Schäffer, "Robot collisions: A survey on detection, isolation, and identification," *IEEE Trans. Robot.*, vol. 33, no. 6, pp. 1292–1312, Dec. 2017.

[11] A. M. Zanchettin, P. Rocco, S. Chiappa, and R. Rossi, "Towards an optimal avoidance strategy for collaborative robots," *Robot. Comput.-Integr. Manuf.*, vol. 59, pp. 47–55, 2019.

[12] S. Haddadin *et al.*, "A truly safely moving robot has to know what injury it may cause," in *Proc. IEEE Int. Conf. Intell. Robots Syst.*, 2012, pp. 5406–5413.

[13] N. Mansfeld, M. Hamad, M. Becker, A. G. Marin, and S. Haddadin, "Safety map: A unified representation for biomechanics impact data and robot instantaneous dynamic properties," *IEEE Robot. Automat. Lett.*, vol. 3, no. 3, pp. 1880–1887, Jul. 2018.

[14] L. Roveda, S. Haghshenas, M. Caimmi, N. Pedrocchi, and L. M. Tosatti, "Assisting operators in heavy industrial tasks: On the design of an optimized cooperative impedance fuzzy-controller with embedded safety rules," *Front. Robot. AI*, vol. 6, no. 75, pp. 1–19,, Aug. 2019.

[15] H. Østerås and T. A. Torstensen, "The dose-response effect of medical exercise therapy on impairment in patients with unilateral longstanding subacromial pain," *Open Orthopaedics J.*, vol. 4, pp. 1–6, 2010.

[16] W. Kim, J. Lee, L. Peternel, N. Tsagarakis, and A. Ajoudani, "Anticipatory robot assistance for the prevention of human static joint overloading in human-robot collaboration," *IEEE Robot. Automat. Lett.*, vol. 3, no. 1, pp. 68–75, Jan. 2018.

[17] L. Peternel, C. Fang, N. Tsagarakis, and A. Ajoudani, "A selective muscle fatigue management approach to ergonomic human-robot co-manipulation," *Robot. Comput.-Integr. Manuf.*, vol. 58, pp. 69–79, 2019.

[18] L. F. Figueredo, R. C. Aguiar, L. Chen, S. Chakrabarty, M. R. Dogar, and A. G. Cohn, "Human comfortability: Integrating ergonomics and muscular-informed metrics for manipulability analysis during human-robot collaboration," *IEEE Robot. Automat. Lett.*, vol. 6, no. 2, pp. 351–358, Apr. 2021.

[19] T. Petrič, L. Peternel, J. Morimoto, and J. Babič, "Assistive arm-exoskeleton control based on human muscular manipulability," *Front. Neurorobot.*, vol. 13, no. 30, pp. 1–10, 2019.

[20] D. Simonetti, L. Zollo, E. Papaleo, G. Carpino, and E. Guglielmelli, "Multimodal adaptive interfaces for 3D robot-mediated upper limb Neuro-Rehabilitation: An overview of Bio-cooperative systems," *Robot. Auton. Syst.*, vol. 85, pp. 62–72, 2016.

[21] F. Scotto di Luzio *et al.*, "Bio-cooperative approach for the human-in-the-loop control of an end-effector rehabilitation robot," *Front. Neurorobot.*, vol. 12, no. 67, pp. 1–12, 2018.

[22] A. Seth *et al.*, "Opensim: Simulating musculoskeletal dynamics and neuromuscular control to study human and animal movement," *PLoS Comput. Biol.*, vol. 14, no. 7, 2018, Art. no. e1006223.

[23] M. Millard, T. Uchida, A. Seth, and S. L. Delp, "Flexing computational muscle: Modeling and simulation of Musculotendon dynamics," *J. Biomechanical Eng.*, vol. 135, no. 2, Feb. 2013, Art. no. 021005.

[24] P. E. Hart, N. J. Nilsson, and B. Raphael, "A formal basis for the heuristic determination of minimum cost paths," *IEEE Trans. Syst. Sci. Cybern.*, vol. 4, no. 2, pp. 100–107, Jul. 1968.

[25] A. Albu-Schaffer, C. Ott, U. Frese, and G. Hirzinger, "Cartesian impedance control of redundant robots: Recent results with the dlr-light-weight-arms," in *Proc. IEEE Int. Conf. Robot. Automat.*, vol. 3, 2003, pp. 3704–3709.

[26] B. Kim and A. D. Deshpande, "An upper-body rehabilitation exoskeleton harmony with an anatomical shoulder mechanism: Design, modeling, control, and performance evaluation," *Int. J. Robot. Res.*, vol. 36, no. 4, pp. 414–435, Apr. 2017.

[27] N. Jarrasse and G. Morel, "Connecting a human limb to an exoskeleton," *IEEE Trans. Robot.*, vol. 28, no. 3, pp. 697–709, Jun. 2012.

[28] A. Schiele and F. C. T. van der Helm, "Kinematic design to improve ergonomics in human machine interaction," *IEEE Trans. Neural Syst. Rehabil. Eng.*, vol. 14, no. 4, pp. 456–469, Dec. 2006.